Geophysical Research Letters

RESEARCH LETTER
10.1029/2024GL109227

The Key Role of Magnetic Curvature Scattering in Energetic Electron Precipitation During Substorms

Ying Zou[1], **Xiao-Jia Zhang**[2,3], **Anton V. Artemyev**[3], **Yangyang Shen**[3], and **Vassilis Angelopoulos**[3]

[1]Applied Physics Laboratory, Johns Hopkins University, Laurel, MD, USA, [2]Department of Physics, The University of Texas at Dallas, Richardson, TX, USA, [3]University of California, Los Angeles, CA, USA

Key Points:

- We investigate the radial location of energetic (50–1,000 keV) electron precipitation (EEP) during a substorm
- We compare the impact of plasma sheet electron precipitation (<30 keV) and EEP (50–1,000 keV) on the altitudinal profile of ionization
- Our results underscore the key role of curvature scattering in energetic electron precipitation during substorms

Supporting Information:

Supporting Information may be found in the online version of this article.

Correspondence to:

Y. Zou,
Ying.Zou@jhuapl.edu

Citation:

Zou, Y., Zhang, X.-J., Artemyev, A. V., Shen, Y., & Angelopoulos, V. (2024). The key role of magnetic curvature scattering in energetic electron precipitation during substorms. *Geophysical Research Letters*, *51*, e2024GL109227. https://doi.org/10.1029/2024GL109227

Received 16 MAR 2024
Accepted 21 JUN 2024

Author Contributions:

Conceptualization: Xiao-Jia Zhang, Anton V. Artemyev
Formal analysis: Ying Zou, Xiao-Jia Zhang, Anton V. Artemyev, Yangyang Shen
Funding acquisition: Xiao-Jia Zhang, Anton V. Artemyev
Investigation: Ying Zou, Xiao-Jia Zhang, Anton V. Artemyev, Yangyang Shen
Methodology: Xiao-Jia Zhang, Anton V. Artemyev
Project administration: Xiao-Jia Zhang, Anton V. Artemyev, Vassilis Angelopoulos
Writing – original draft: Ying Zou, Xiao-Jia Zhang, Anton V. Artemyev
Writing – review & editing: Ying Zou, Xiao-Jia Zhang, Anton V. Artemyev, Yangyang Shen, Vassilis Angelopoulos

Abstract

Energetic electron precipitation (EEP) during substorms significantly affects ionospheric chemistry and lower-ionosphere (<100 km) conductance. Two mechanisms have been proposed to explain what causes EEP: whistler-mode wave scattering, which dominates at low latitudes (mapping to the inner magnetosphere), and magnetic field-line curvature scattering, which dominates poleward. In this case study, we analyzed a substorm event demonstrating the dominance of curvature scattering. Using ELFIN, POES, and THEMIS observations, we show that 50–1,000 keV EEP was driven by curvature scattering, initiated by an intensification and subsequent earthward motion of the magnetotail current sheet. Using a combination of Swarm, total electron content, and ELFIN measurements, we directly show the location of EEP with energies up to ~1 MeV, which extended from the plasmapause to the near-Earth plasma sheet (PS). The impact of this strong substorm EEP on ionospheric ionization is also estimated and compared with precipitation of PS (<30 keV) electrons.

Plain Language Summary

During magnetospheric substorms, energetic electrons in the Earth's plasma sheet (PS), the night-side magnetosphere region filled by hot plasma, precipitate to the ionosphere. Energetic electron precipitation (EEP) affects the density, temperature, and composition of the ionosphere. However, the exact process that causes such precipitation is not well understood due to observational constraints. The challenge lies in simultaneously measuring the EEP properties at the ionosphere and the plasma and wave properties in the PS. We analyze a fortuitous satellite conjunction during a substorm, during which EEP was simultaneously captured by ELFIN, Swarm, and POES at low altitudes, and THEMIS in the equatorial PS. EEP was observed to extend across a broad equatorial domain, projecting into a wide ionospheric region and encompassing the PS region and a significant portion of the inner magnetosphere. High-energy-resolution measurements from ELFIN reveal that the main driver of precipitation is the scattering of energetic electrons by strongly curved magnetic field lines in the PS, as opposed to the more commonly suggested scattering mechanisms associated with wave-particle interactions. We also show that the EEP drastically altered the ionization profile of the ionosphere.

1. Introduction

The magnetospheric substorm is a fundamental component of geomagnetic activity, resulting in rapid energization of charged particles in the near-Earth magnetotail (see reviews by Birn et al., 2021; Sitnov et al., 2019, and references therein), followed by their subsequent injection into the inner magnetosphere (see reviews by Baker et al., 1996; Gabrielse et al., 2022, and references therein). Energetic ions drift duskward, contributing to magnetosphere-ionosphere coupling, through processes such as sub-auroral polarization streams (SAPS) (see review Mishin & Streltsov, 2021, and references therein). Conversely, energetic electrons drift dawnward and contribute, through their scattering and precipitation, to ionization and heating of the ionosphere (C. J. Rodger et al., 2022; Thorne et al., 2010). Substorm injections are mesoscale and transient phenomena (e.g., Gabrielse et al., 2014; Nakamura et al., 2002; Sorathia et al., 2021). While the importance of substorm injection energy input into the ionosphere has been recognized and actively investigated (see review Gabrielse et al., 2022; Jordanova et al., 2023; Yu et al., 2022, and references therein), quantifying it is challenging due to the transient nature of injections (see discussions in Heelis & Maute, 2020; C. Huang, 2021).

A crucial element of substorm injections is the energetic electron precipitation (EEP) into the ionosphere (e.g., Gabrielse et al., 2019; Gkioulidou et al., 2012; Sergeev et al., 2020). Depending on their energy, precipitating electrons can penetrate down to the E/D-layer (below 80 km, see Nikolaev et al., 2021; Oyama et al., 2017;

Stepanov et al., 2021), where they can impact ionospheric chemistry (Mironova et al., 2019; Seppälä et al., 2015; Verronen et al., 2021), lead to mesospheric ozone loss (Chapman-Smith et al., 2023), increase local conductance (Yu et al., 2018), and contribute to large-scale ionosphere disturbances (Lyons et al., 2021; Nishimura et al., 2021).

The spatial localization (in MLT) of substorm EEP in the post-midnight/dawn sector (C. J. Rodger et al., 2022) suggests that these electrons are likely scattered into the ionosphere via resonant interactions by whistler-mode waves (WW) (at lower *L*-shells) (Thorne et al., 2010; Yu et al., 2018) or via curvature scattering in the magnetotail current sheet (at higher *L*-shells) (Sivadas et al., 2017; Yahnin et al., 2016). Relativistic electron scattering by electromagnetic ion cyclotron waves around midnight may also contribute to EEP (Capannolo et al., 2022; Hendry et al., 2021; Yahnin et al., 2017). Due to the low-energy resolution of measurements from the POES (NOAA/MetOp) satellite fleet (Evans & Greer, 2004; Green, 2013), which has been the predominant source of EEP observations, and the large mapping uncertainties from low altitudes to the nightside magnetotail (see discussions in Artemyev et al., 2022; Sergeev et al., 2011), the *L*-shell and primary drivers of substorm EEP are still under investigation (see, e.g., discussions in Bland et al., 2021; Cresswell-Moorcock et al., 2013; Sivadas et al., 2019).

In this study, we investigate substorm EEP by combining ELFIN CubeSats (Angelopoulos et al., 2020) measurements with near-equatorial THEMIS (Angelopoulos, 2008) measurements, as well as low-altitude Swarm (Olsen et al., 2013) and POES (Dichter et al., 2015) measurements. We demonstrate that the dominant mechanism of EEP is likely curvature scattering. Through a combination of ELFIN measurements and the auroral (<30 keV) electron precipitation model of OVATION prime (Newell et al., 2009), we show the pivotal role of curvature scattering in influencing EEP impacts on the ionosphere at < 100 km altitude during prolonged intervals of substorms.

2. Spacecraft Observations

Figure 1 shows an overview of the near-equatorial spacecraft observations for the event on 07 August 2021. Geomagnetic activities remained consistently elevated from 00:00 to 05:00 UT, with AE index reaching a maximum of 600 nT and remaining above 200 nT throughout. Sym-H index maintained the value of ∼−30 nT during the entire interval, indicative of a ring current ion population likely supplemented by new injections. Indeed, THEMIS E in the post-midnight sector and GOES 16 in the pre-midnight sector detected several substorm injections (around 00:15 UT, 01:00–02:00 UT, 03:00–04:00 UT, and 05:00 UT, see panels (f, g)), manifested as increases in energetic electron fluxes (measured by the THEMIS solid state telescope; see Angelopoulos et al., 2008) and energetic ion flux (measured by GOES space weather suite of instruments; see Boudouridis et al., 2020; Dichter et al., 2015), respectively. During 00:00–05:00 UT, THEMIS E traversed around the equator (panel (b) shows that B_x measured by the fluxgate magnetometer, Auster et al., 2008, is around zero) from the PS to lower *L*-shells, and finally crossed the plasmapause around 05:20UT (shown by the plasma density gradient in panel (b) derived from the spacecraft potential; see methodology details in Bonnell et al., 2008; Nishimura et al., 2013). The plasmapause was also associated with a strong gradient in PS electron fluxes (panel (d)) and an energy dispersion in ion fluxes (panel (e)), as observed by the THEMIS electrostatic analyzer (see McFadden et al., 2008). Closer to the plasmapause (04:00–05:00 UT), THEMIS E detected chorus waves, characterized by narrow-band wave emissions bounded by the lower hybrid frequency, f_{lh}, and half the local electron gyrofrequency, f_{ce}. These waves are commonly observed in the post-midnight sector during substorms (Agapitov et al., 2013; Meredith et al., 2012) and drive electron precipitation (see, e.g., reviews by Shprits et al., 2008; Thorne et al., 2021, and references therein).

To investigate EEP, we combine measurements from: (a) low-altitude (∼450 km) ELFIN CubeSats (Angelopoulos et al., 2020) providing 1.5s-resolution precipitating (within the local loss cone, j_{prec}) and locally trapped (outside of the local loss cone, j_{trap}) electron fluxes at 50–6000 keV, in 16 logarithmically distributed energy channels, (b) low-altitude (∼850 km) POES (NOAA/MetOp) satellites (Evans & Greer, 2004; Green, 2013) providing 1s-resolution precipitating and trapped proton (30–80 keV) and electron (>30 keV) fluxes, (c) low-altitude (∼460–530 km) Swarm satellites (Olsen et al., 2013) providing electron density and temperature, and ion drift velocity (Knudsen et al., 2017; Lomidze et al., 2018). Figure 2 shows ELFIN measurements during six orbits alongside POES (NOAA/MetOp) and Swarm measurements around the same times; the data are shown as a function of magnetic latitude.

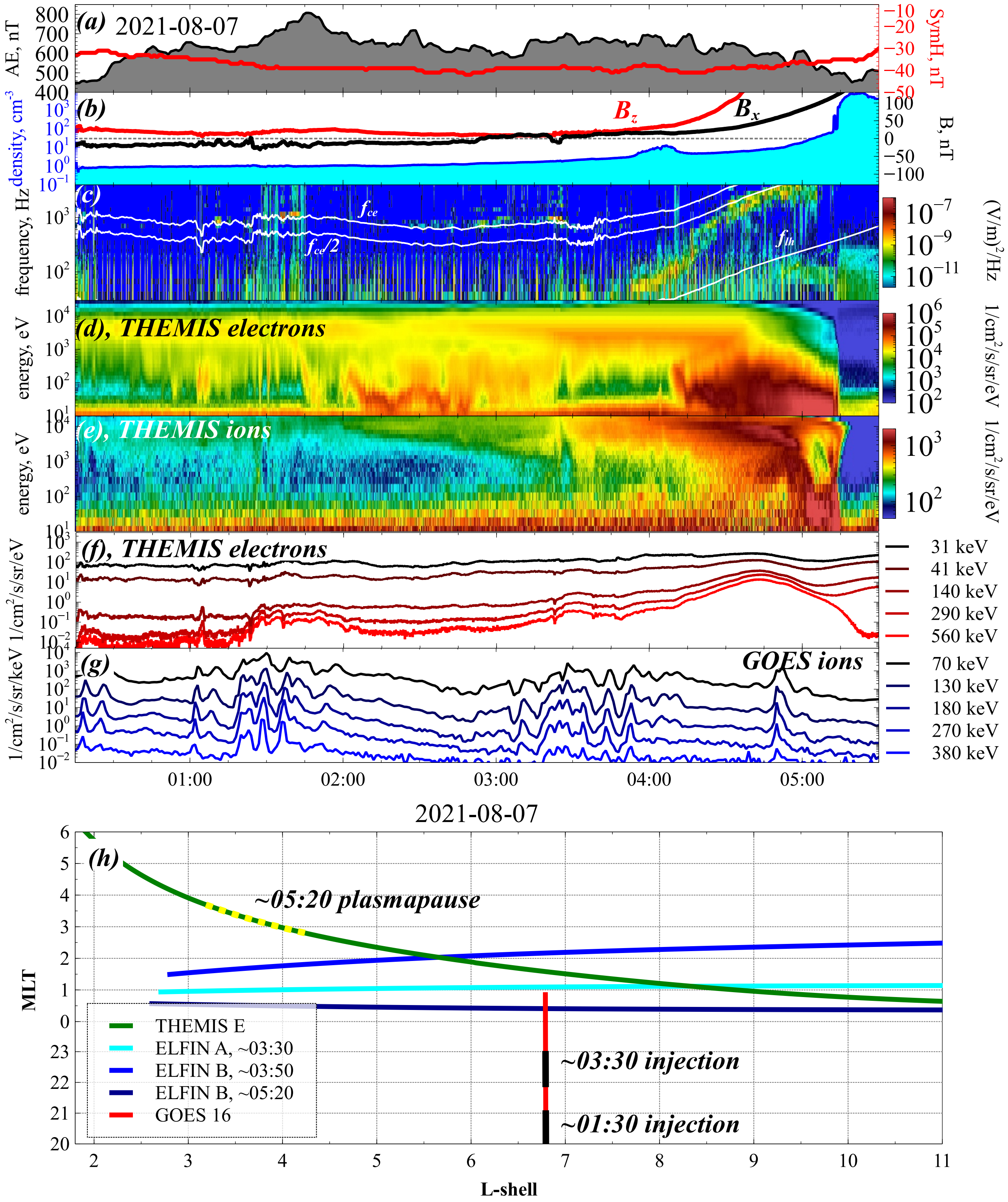
(a) 2021-08-07
AE, nT
SymH, nT
(b)
density, cm^{-3}
B_z
B_x
B, nT
(c)
frequency, Hz
f_{ce}
$f_{ce}/2$
f_{lh}
(V/m)^2/Hz
(d), THEMIS electrons
energy, eV
1/cm^2/s/sr/eV
(e), THEMIS ions
energy, eV
1/cm^2/s/sr/eV
(f), THEMIS electrons
1/cm^2/s/sr/eV
31 keV
41 keV
140 keV
290 keV
560 keV
(g)
GOES ions
1/cm^2/s/sr/keV
70 keV
130 keV
180 keV
270 keV
380 keV
01:00
02:00
03:00
04:00
05:00
2021-08-07
(h)
~05:20 plasmapause
MLT
THEMIS E
ELFIN A, ~03:30
ELFIN B, ~03:50
ELFIN B, ~05:20
GOES 16
~03:30 injection
~01:30 injection
L-shell

Figure 1.

Let us illustrate the data format using the first orbit (1) from 00:40 to 00:46 UT, which falls within the quiet interval before EEP observations. Panels (a) and (b) show Swarm measurements of electron density, temperature (in red), and ion drift velocity. The density gradient around $|MLAT| \sim 61°$ likely represents the low-altitude projection of the plasmapause (see, e.g., Heilig et al., 2022), which approximately coincides with the projection of equatorial plasmapause measurements from THEMIS (green dashed box). Poleward of this gradient, $|MLAT| > 61°$, Swarm detected density and temperature fluctuations, with an enhanced electron temperature. This region encompasses the outer radiation belt and near-Earth PS, with expected PS electron precipitation (likely providing ionosphere heating, see Bekerat et al., 2007; Khazanov et al., 2020). The density depletion and temperature increase around $|MLAT| \sim 59°$ likely represent the extension of the duskside density depletion resulting from flow stagnation and/or duskside SAPS (Aa et al., 2020; Pryse et al., 2006; A. Rodger, 2008). To show the EEP location relative to the ionospheric density structure, we overlay all ELFIN and Swarm orbits onto a simultaneous total electron content (TEC) map, which reveals the counterpart of the plasmapause, known as the mid-latitude ionospheric trough—a localized minimum in TEC (see A. Rodger, 2008; Vo & Foster, 2001; Yizengaw & Moldwin, 2005). Figures S1–S5 in Supporting Information S1 and bottom panel of Figure 2 consistently demonstrate that the EEP is located just poleward of the plasmapause (TEC minimum).

Figure 2(1b) shows ion drifts revealing the formation of polarization streams, which are strong ionosphere plasma flows driven by electric fields associated with plasma injections into the inner magnetosphere (see Califf et al., 2022; Lejosne et al., 2018; Mishin & Streltsov, 2021). While the most extensively studied polarization streams, such as SAPS including sub-auroral ion drifts (Foster & Vo, 2002; Galperin et al., 1973; Spiro et al., 1978), are typically observed at the dusk flank (see statistics in He et al., 2014; Nishimura et al., 2022), there are recent reports of dawnside auroral polarization streams (Liu et al., 2020) and classical SAPS extending to the dawn flank during periods of high geomagnetic activity (e.g., magnetospheric storms, see Horvath & Lovell, 2023; C.-S. Huang et al., 2021; Lin et al., 2022). Therefore, we use the ion drift velocity to detect the formation of polarization streams during EEP events. For each ELFIN orbit, we use nearby measurements from Swarm A or B, whichever is closest to ELFIN.

For each ELFIN orbit, we show observations from the POES (NOAA/MetOp) satellite (with the smallest time and MLT separation from ELFIN) to infer the proton isotropy boundary (see details in Dubyagin et al., 2002; Sergeev et al., 2015), the transition between isotropic fluxes (when the solid black line of locally trapped proton fluxes is close to the upper edge of the gray region representing precipitating fluxes) presumbably from the PS and anisotropic fluxes (when the solid black line is well above the upper edge of the gray region) presumably from the inner magnetosphere. This transition defines the inner edge of the ion PS (Newell et al., 1998; Sergeev et al., 2012; Yahnin et al., 1997). The red solid and dashed lines show locally trapped and precipitating electron fluxes, respectively. They serve to examine the quality of the POES-ELFIN conjunction by ensuring the isotropy boundary for ∼30–100 keV electrons is seen at approximately the same magnetic latitude at the two spacecraft. In Figure 2(1c), the ion and electron isotropy boundaries are at ∼61° and ∼63°, respectively.

Figure 2(1d,e) show ELFIN measurements of j_{trap} and j_{prec}/j_{trap} ratio. From left to right: (a) ELFIN traverses the plasmasphere (from 55.5° to ∼58.5°) with only trapped electrons and a low level of relativistic electron fluxes, (b) ELFIN enters the outer radiation belt (from 58.5° to ∼63°) characterized by strong trapped fluxes of relativistic electrons and weak precipitation, likely resulting from electron scattering by WW, (c) ELFIN reaches the PS (>∼63°) where only <300 keV fluxes are observed, with strong curvature scattering that fills the loss cone. ELFIN detects the transition between weak and strong electron precipitation at ∼63°, where both NOAA-19 and ELFIN identify the electron isotropy boundary. The electron isotropy boundary can also be interpreted as the inner boundary of curvature scattering, with EEP equatorward of this boundary facilitated by whistler-mode wave scattering.

Subinterval (1) in Figure 2 shows a quiet period devoid of EEP activity. Panels (2) present observations from Swarm A, NOAA-18, and ELFIN A at the onset of the active period, immediately following the first large

Figure 1. Overview of equatorial measurements (from THEMIS-E and GOES-16) during a sub-auroral polarization streams event on 07 August 2021: (a) AE and Sym-H geomagnetic indexes, (b) two magnetic field components and plasma density inferred from THEMIS spacecraft potential, (c) wave electric field in the 30–4,000 Hz frequency range (white horizontal traces from top to bottom show electron cyclotron frequency f_{ce}, $f_{ce}/2$, and f_{lh}), omnidirectional (d) electron and (e) ion fluxes from THEMIS ESA (<30 keV), (f) omnidirectional electron fluxes from THEMIS SST, (g) GOES-16 energetic proton fluxes, (h) projections of THEMIS E, GOES-16, ELFIN A and B orbits to the equator.

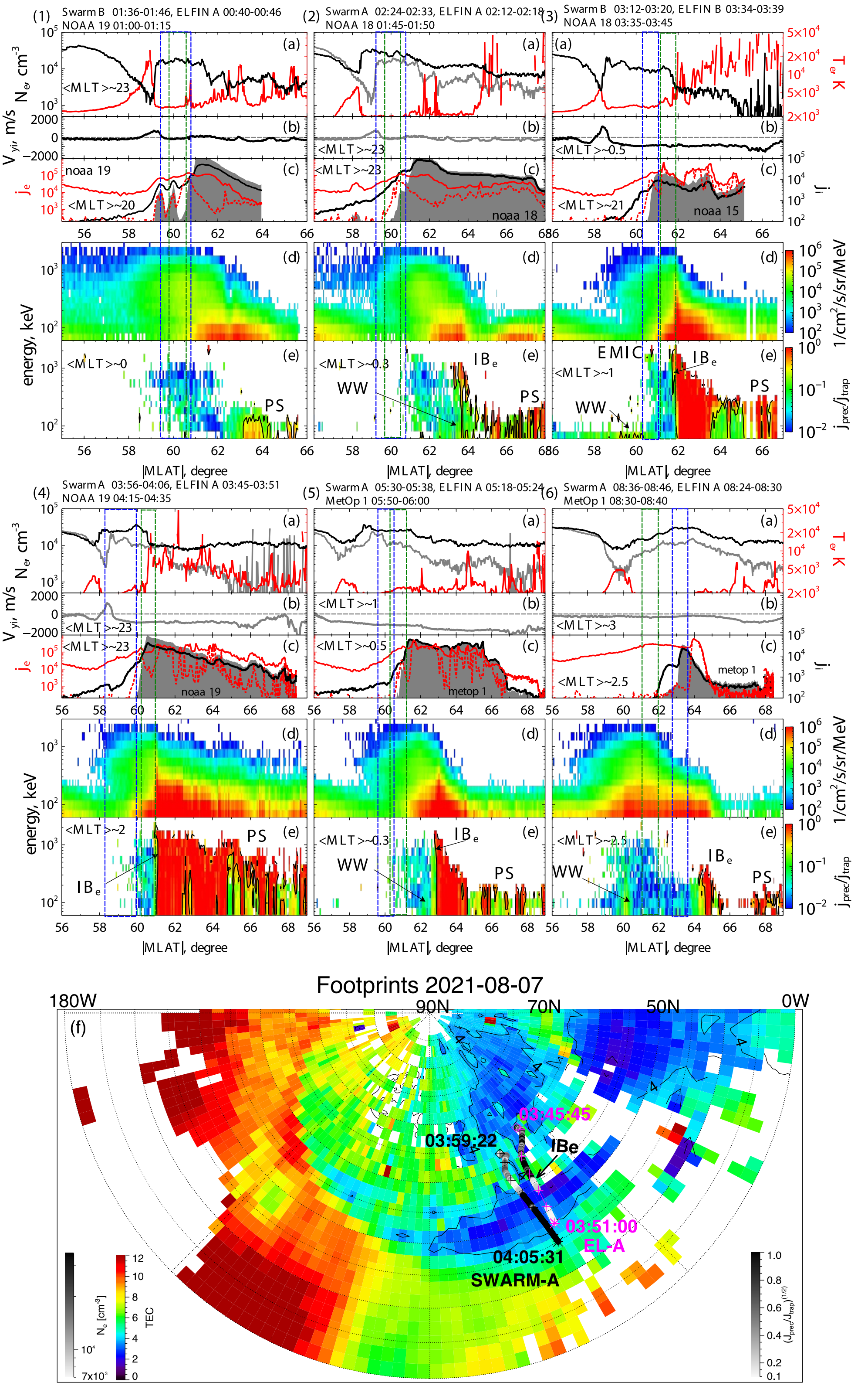
(1) Swarm B 01:36-01:46, ELFIN A 00:40-00:46
NOAA 19 01:00-01:15
(2) Swarm A 02:24-02:33, ELFIN A 02:12-02:18
NOAA 18 01:45-01:50
(3) Swarm B 03:12-03:20, ELFIN B 03:34-03:39
NOAA 18 03:35-03:45
(4) Swarm A 03:56-04:06, ELFIN A 03:45-03:51
NOAA 19 04:15-04:35
(5) Swarm A 05:30-05:38, ELFIN A 05:18-05:24
MetOp 1 05:50-06:00
(6) Swarm A 08:36-08:46, ELFIN A 08:24-08:30
MetOp 1 08:30-08:40
|MLAT|, degree
energy, keV
EMIC
IBe
WW
PS
Footprints 2021-08-07
180W
90N
70N
50N
0W
03:45:45
03:59:22
IBe
03:51:00
EL-A
04:05:31
SWARM-A
TEC

Figure 2.

injection detected by GOES-16 and THEMIS E (see Figure 1). NOAA-18 identified the ion isotropy boundary at ∼61°, consistent with observations 90 min prior (compare (1c) and (2c) in Figure 2). ELFIN A detected the electron isotropy boundary at ∈ [63, 64]°. In contrast to the previous orbit, the precipitating electron energy increased to ∼1 MeV (compare (1e) and (2e) in Figure 2). Additionally, the PS region (poleward from ∼65°) exhibited higher fluxes and stronger precipitation (compare (1d,e) and (2d,e) in Figure 2).

The most geomagnetically active period occurred between 03:00UT and 05:30UT (see Figure 2(3–5)). During the first two orbits (3 and 4), Swarm detected an ionosphere density gradient around $|MLAT| \sim$ 61–62°, close to the projection of THEMIS E observed plasmapause (see Figure 2(3a–5a)), but this gradient is less discernible during orbit (5). Poleward from the plasmapause, Swarm observed significant perturbations in electron temperature (Panels 2(3a, 4a, 5a)), likely driven by PS (≤1 keV; not measured by ELFIN) electron precipitation (e.g., Bekerat et al., 2007; Khazanov et al., 2020). Swarm B also detected strong eastward ion flows (1,000–2,000 km/s) with a very wide latitudinal extent, encompassing the plasmasphere and PS (see Figure 2(3b,5b)). These flows can be attributed to dawnside SAPS (observed during geomagnetically active times, e.g., storms; see Horvath & Lovell, 2023; C.-S. Huang et al., 2021). Indeed, the ion injection detected by GOES-16 around 03:30 UT (see Figure 1g) could, if sufficiently strong, contribute to SAPS formation post-midnight (see simulation results in Lin et al., 2022). Additionally, the poleward part of this enhanced ionospheric flow may also be attributed to a SAPS, previously associated with fast flows in the near-Earth PS (e.g., Liu et al., 2020).

Observations from NOAA-15, NOAA-19, and MetOp-1 reveal that both the ion and electron isotropy boundaries have shifted equatorward to 60–62° and almost coincide with the plasmapause (see Figure 2(3c–5c)). ELFIN observations of the electron isotropy boundary confirm its location within 60–62° (see Panels 2 (3e, 4a, 5e)). Therefore, the inner edge of the ion and electron PS lies close to the plasmapause, completely encompassing the outer radiation belt. Notably, this inner edge is expected to exhibit a very strong radial gradient of the equatorial magnetic field B_z (see discussions of the relation between the latitudinal extent of the isotropy boundary and equatorial magnetic field profile in Sergeev et al., 2018), because the ion and electron isotropy boundaries are separated by about one degree in latitude (see Panels 2(3c, 4c, 5c)) and isotropy boundaries of 50 keV and 1 MeV electrons are separated by less than one degree in latitude (see Panels 2(3e, 4e, 5e)). Indeed, equatorial THEMIS E observations indicate an increase in B_z from ≤10 nT to ∼100 nT within ∼1.5 Earth radii (03:00–04:30 UT), just before encountering the plasmapause. Poleward from the electron isotropy boundary, ELFIN detected a region of EEP spanning several degrees in latitude (see Figure 2(4d,e)). This is consistent with previous reports of the latitudinal extent of EEP (see Bland et al., 2021, 2022; Yu et al., 2018). The upper energy range of EEP is ∼1 MeV near the electron isotropy boundary and goes down to 300 keV poleward. However, during the most intense EEP interval (see Figure 2 (4d,e)), the latitudinal range [61°, 67°] is filled with ∼500 keV EEP. This upper energy limit of EEP at ∼1 MeV exceeds the ∼200–500 keV range reported by Miyoshi et al. (2015); Turunen et al. (2016); Oyama et al. (2017), but agrees with the estimates from Tesema et al. (2020).

To verify the positions of the precipitation region, we project Swarm and ELFIN orbits onto TEC maps. The Supporting Information shows such projections for all intervals from Figure 2 (see Figures S1–S5 in Supporting Information S1), whereas the bottom panel of Figure 2 exemplifies the most intense EEP interval (4). Swarm A and ELFIN A orbits closely align, and the electron isotropy boundary (IBe; seen at ELFIN as a

Figure 2. Six subintervals of Swarm A, B, ELFIN A, B, and NOAA/MetOp observations during the event presented in Figure 1. In each subinterval, we show the following: (a) Swarm plasma density (black) and electron temperature (in Kelvin, red). (b) Ion horizontal drift velocity (black). Note that if Swarm A lacks reliable ion drift measurements, we show Swarm B data from the nearest orbit (but density and velocity are in gray, instead), (c) NOAA/MetOp measurements of 30–80 keV precipitating (gray shaded area) and trapped (black line) proton fluxes, and >30 keV precipitating (dashed red) and trapped (solid red) electron fluxes. (d) ELFIN spectra of locally trapped electrons and (e) of electron precipitating-to-trapped flux ratio. Blue dashed boxes in each subinterval show the location of proton isotropy boundary inferred from NOAA/MetOp measurements. Green dashed boxes in each subinterval show the projection of the equatorial location of the plasmapause traversed by THEMIS E around 05:10UT. Typical patterns of electron precipitation are indicted: curvature scattering within the plasma sheet, electron isotropy boundary (IBe), relativistic electron precipitation driven by electromagnetic ion cyclotron waves (EMIC), and energetic electron precipitation driven by whistler-mode waves. For each satellite, the average MLT is tabulated in the respective panels, while the UT is listed at the top. The bottom panel shows projections of ELFIN-A and Swarm-A orbits onto the total electron content (TEC) map for interval (4). Diamonds and asterisks mark the start and end times of the trajectories, crosses represent 1-min tickmarks, and the line is color-coded by j_{prec}/j_{trap} of 100 keV electrons for ELFIN and by ionosphere density N_e for Swarm. Location of the electron isotropy boundary (IBe) is indicated by a black arrow. TEC data gaps, resulting from a lack of Global Navigation Satellite System ground receivers, are shown as white. Similar projections for other intervals can be found in the Supporting Information (Figures S1–S5 in Supporting Information S1).

10.1029/2024GL109227

sharp change in the precipitating-to-trapped flux ratio, indicated by color along the orbit) almost coincides with the sharp change in the ionosphere density measured by Swarm (shown by color along the orbit). This density gradient likely corresponds to the ionosphere projection of the plasmapause. East side from Swarm and ELFIN orbits, TEC shows the typical dusk-side pattern with the mid-latitude ionospheric trough–a localized minimum in TEC associated with the plasmapause projection to low altitudes (see A. Rodger, 2008; Vo & Foster, 2001; Yizengaw & Moldwin, 2005). Conversely, on the dawn side (where ELFIN observed EEP), the TEC minimum is broad and extends to high latitudes, with a localized enhancement polerward from IBe. Therefore, IBe and the density gradient detected by Swarm lie at the poleward edge of the dusk-side continuation of the mid-latitude ionospheric trough (this broadly aligns statistical results indicating that the plasmapause is located polerward from the TEC minimum on the dawn side, see Shinbori et al., 2021).

Figure 2(3–5) illustrate a prolonged (at least ~2 hr), latitudinally extended (up to $\Delta MLAT \sim 7°$) EEP event, exhibiting relativistic energies. The entire region of enhanced precipitation-ratio associated with this EEP interval lies poleward of the electron isotropy boundary and exhibits higher precipitation-ratio at >500 keV than at ~100 keV (see Figure 2(4), at $|MLAT| > 62°$). This precipitation cannot be attributed to WW because whistler-mode wave driven precipitation would be expected to occur equatorward of the isotropy boundary and to exhibit stronger precipitating-to-trapped ratios at lower energies than at higher energies (see details in Gan et al., 2023; Tsai et al., 2022). Weaker precipitation events due to WW, marked as *WW*, are observed equatorward from the isotropy boundary. An important feature of strong EEP polerward from the isotropy boundary is the increase in the precipitating-to-trapped flux ratio with energy, which can be clearly seen in, for example, ~63.5° in (3e), ~65.5° in (4e), ~66.2° in (5e) (see also Figure S12 in Supporting Information S1, where individual spectra of precipitating-to-trapped flux ratio are shown). Such dispersive precipitation, starting from relatively low energies (~50 keV, well below the range of precipitation attributed to electromagnetic ion cyclotron waves (Summers & Thorne, 2003)), is consistent with field-line curvature scattering, which is expected to occur poleward of the isotropy boundary at all energies where sufficient equatorial fluxes are available. The fundamental property of this scattering mechanism is its strong dependence on the ratio of the curvature radius of magnetic field lines to the particle gyroradius, that is, larger gyroradius (corresponding to higher energy) results in stronger scattering (see, e.g., model in Young et al., 2002, and references therein). These EEP characteristics, epitomize the dominant role of curvature scattering in electron precipitation during substorm times, compared to whistler-mode wave scattering. Figure 2(6) shows post-substorm quiet-time ELFIN observations, where EEP from the PS returns to the pre-substorm level seen around 00:40–02:10UT during the first two ELFIN orbits.

We now investigate the impact of the observed EEP during 03:30–05:30 UT (refer to Figure 2(3–5)) on Earth's ionosphere. To determine the entire precipitation spectrum, we combine ELFIN measurements (>50 keV) with the OVATION prime model (Newell et al., 2002, 2014) providing <30 keV flux parameters for OMNI database input (King & Papitashvili, 2005). For each ELFIN orbit from Figure 2 we obtain a kappa (power-law) distribution function for <30 keV precipitating electrons (see Khazanov et al., 2018, 2021) and fit this distribution and the ELFIN spectra by a single kappa function to cover the gap [30,50]keV. We also obtain Maxwelling distribution from OVATION model. Details of the fitting process and results are available in Supporting Information, Figures S6–S11 in Supporting Information S1. We obtained these distributions for two intervals of $\Delta MLAT = 1°$ during each ELFIN orbit: one around the electron isotropy boundary and one slightly poleward of it. Panels (a, b) in Figure 3(1–6) show the OVATION-only derived Maxwellian (black) and kappa (red/magenta) distributions at energies <30 keV, and the actual ELFIN electron precipitation measurements at >50 keV (solid red or magenta lines, for the two time-intervals respectively). Additionally, the same panels show the combined OVATION-ELFIN fits (dashed lines) covering the entire spectrum of precipitating electrons of interest, between $[10^{-1}, 10^{3}]$ keV. Using that we estimate the vertical profile of the ionization rate due to EEP (see Supporting Information and Fang et al. (2010)) using the Maxwellian fits only as inputs (black dashed lines in Figure 3(3c–5c)) and using the kappa fits to the combined OVATION prime parameters and the ELFIN spectra data (red and magenta lines, for the two times, respectively, in Figure 3(3c–5c)). The first two ELFIN orbits and the last orbit from Figure 2, when EEPs were weak, do not exhibit significant impacts of ELFIN-measured, >50 keV fluxes on the ionization rate profile: red and magenta curves show similar intensities and altitudes of the ionization peak around ~110–120 km, whereas the ionization below this peak due to >50 keV electrons quickly decreases with altitude (see Figure 3(1,2,6)). However, subintervals (3–5) of Figure 2

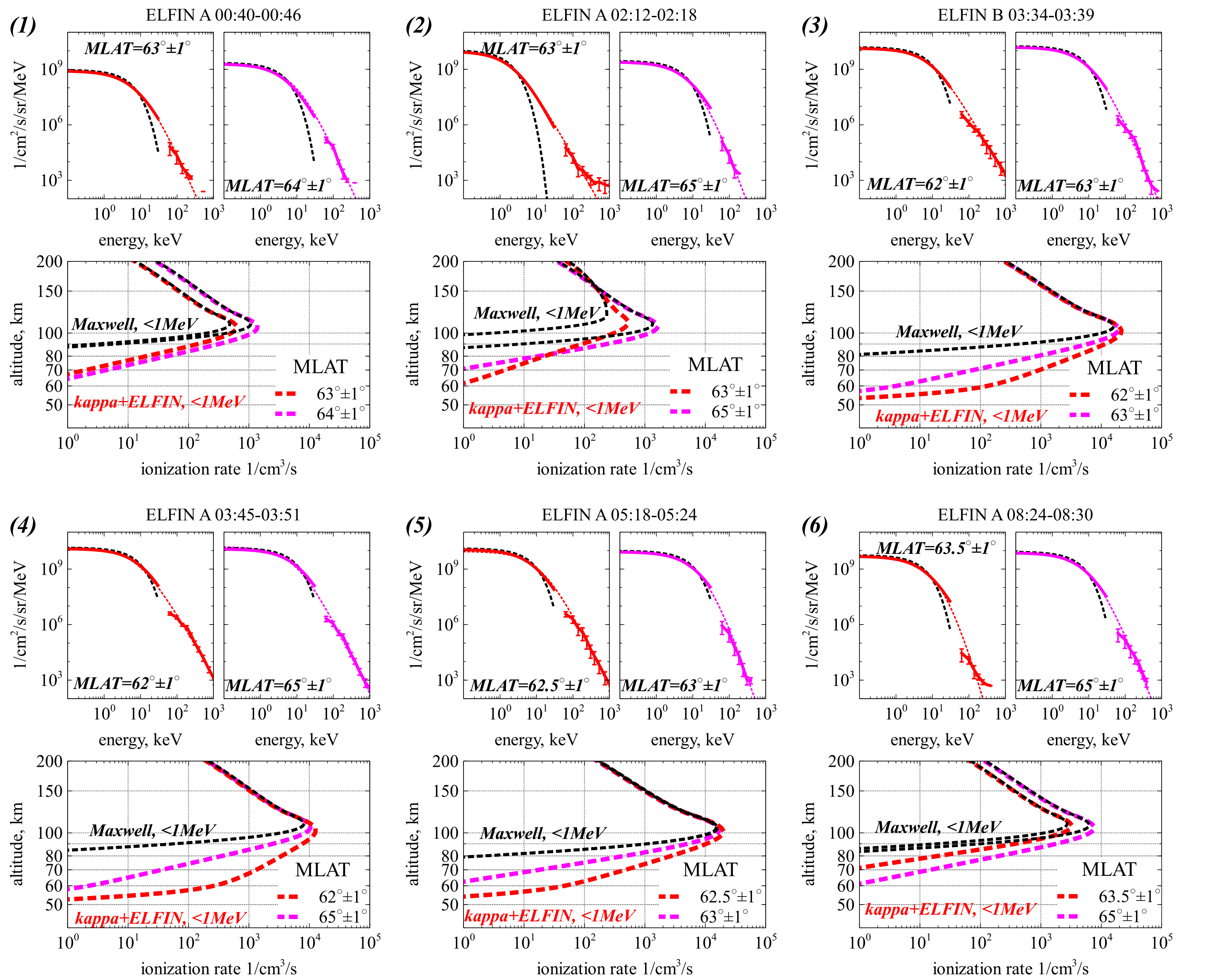

Figure 3. Overview of the ionization rate profiles due to EEP during the six subintervals of Figure 2. For each subinterval, we show two examples of precipitating spectra (two top panels) and four examples of ionization rate altitude profiles (bottom single panel). In the energy spectra (two top panels), OVATION-only model spectra are depicted as Maxwellian fits to OVATION parameters (dashed black curves) and as power-law (kappa function) fits to the same parameters (solid lines, red and magenta for the two times, respectively). In the same panels, EEP spectra measured by ELFIN (>50 keV, solid lines, red and magenta for the two times respectively) are shown with error bars, depicting the standard deviation of the fluxes within $\Delta MLAT = 1°$. Fits to both OVATION-model parameter and ELFIN spectra (dotted lines, red and magenta for the two times, respectively) also shown. The ionization rate altitude profiles (bottom single panel) derived from the above spectra as inputs are shown for Maxwellian fits (dashed black lines for the two times) and combined OVATION-ELFIN data fits (dashed lines, red and magenta for the two times, respectively). Figures S6–S11 in Supporting Information S1 further expand on the fitting procedure. Note although the Maxwellian fit is based on <30 keV electron flux from OVATION model, we extrapolate it to 1 MeV to compare with measurements from ELFIN. Due to the rapid flux decrease with energy in this fit, there barely is any impact of >30 keV electrons on the ionization rate.

show a very different behavior. As shown in Figure 3(3c–5c), strong EEPs with energies reaching 1 MeV significantly alter the ionization profile: the ionization peak in red/magenta curves (full fits) are stronger by a factor of ×3 and ~10 km lower in altitude than the peaks of the black curves. The ionization rates below the peak, in the range [60,100] km (due to > 50 keV precipitation) decreases much more slowly with decreasing altitude during the substorm, that at times before and after.

3. Conclusions

In this study, we analyzed a roughly 2-hr long EEP event observed by ELFIN in the post-midnight sector. During this event, electron precipitation extends to relativistic energies, reaching up to approximately ~1 MeV, which can contribute to ionization down to the 60 km altitude. The latitudinal extent of the relativistic EEP spans ~7° in magnetic latitudes, covering a broad region from the plasmapause to the near-Earth PS. High-energy-resolution measurements from ELFIN reveal that the dominant mechanism for EEP is curvature scattering. This is evident from the distinct energy dispersion of the EEP boundary, coinciding with the electron isotropy boundary. Moreover, the ratio of precipitating-to-trapped flux increases with the energy increase, with stronger precipitation at higher energies, as shown in Figure 2(4). This, in turn, suggests two things: (a) the current sheet, the primary region of curvature scattering, has shifted earthward, nearing the plasmapause, thereby providing strong precipitation of relativistic electrons previously residing in the outer radiation belt; (b) EEP from the PS is considerably weaker that from the inner magnetosphere, as is especially evident in sub-intervals (3,5) from Figure 2, indicating a localized latitudinal (radial) extent of the EEP region. These effects, driven by the current sheet's earthward motion and the localized nature of curvature scattering-induced EEP, demonstrate a novel mechanism for intense EEP during substorms, distance from wave-particle resonant interactions. Future investigations with comprehensive spacecraft coverage of the near-Earth PS region are warranted to further explore these phenomena.

The comparison of ionization rate altitude profiles arising from auroral electron precipitation (<30 keV) and from the entire precipitation spectrum (up to ~1 MeV) highlights the importance of relativistic EEP in shaping the ionization profile. The fine structure of EEP, both in terms of energy and latitudinal extent, suggests that the current POES-based EEP parameterization (e.g., Z. Chen et al., 2023; H. Chen et al., 2023) could benefit significantly from including high-resolution differential energy flux measurements obtained from ELFIN. Furthermore, ELFIN observations of substorm EEP offer valuable opportunities to validate existing EEP models (Beharrell et al., 2015; Mukhopadhyay et al., 2022).

Acknowledgments

We are very grateful to Dr. Xing Meng (Jet Propulsion Laboratory, California Institute of Technology) for providing TEC data set, helpful discussion, and detailed suggestions of TEC data interpretation, which make this study possible. We are grateful to NASA's CubeSat Launch Initiative for ELFIN's successful launch in the desired orbits. We acknowledge early support of ELFIN project by the AFOSR, under its University Nanosat Program, UNP-8 project, contract FA9453-12-D-0285, and by the California Space Grant program. We acknowledge critical contributions by numerous ELFIN team members and support by NASA 80NSSC22K1005 and NSF Grants AGS-1242918, AGS-2019950. We acknowledge NASA contract NAS5-02099 for the use of data from the THEMIS Mission. GPS TEC data products and access through the Madrigal distributed data system are provided to the community by the Massachusetts Institute of Technology (Haystack GPS PI, Anthea Coster). We acknowledge the Swarm mission and data center operated by ESA. Y. Zou and X.-J. Z. acknowledge support from the NASA Grant 80NSSC24K0138. A.V.A and X.-J. Z. acknowledge support from the NASA Grants 80NSSC20K1270, 80NSSC24K0561. X.-J. Z. acknowledges support from the NSF Grant 2329897. V. A. acknowledges support by NSF award AGS-2019950 and NASA contract NAS5-02099. Part of this research was carried out at the Jet Propulsion Laboratory, California Institute of Technology, under a contract with the National Aeronautics and Space Administration (80NM0018D0004).

Data Availability Statement

Fluxes measured by ELFIN are available in ELFIN data archive https://data.elfin.ucla.edu/ in CDF format. Total electron content maps are provided by MIT Haystack via the Madrigal database http://cedar.openmadrigal.org; see Rideout and Coster (2006); Coster et al. (2013); Vierinen et al. (2015). Fluxes measured by POES/MetOp satellites are available in NOAA data archive https://www.ngdc.noaa.gov/stp/satellite/poes/dataaccess.html in CDF format. Magnetic field, plasma density, and ion drift speed measured by Swarm satellites are available in ESA data archive https://swarm-diss.eo.esa.int/. Data analysis was done using SPEDAS V4.1 (Angelopoulos et al., 2019). The software can be downloaded from http://spedas.org/wiki/index.php?title=Downloads_and_Installation.

References

Aa, E., Zou, S., Erickson, P. J., Zhang, S.-R., & Liu, S. (2020). Statistical analysis of the main ionospheric trough using Swarm in situ measurements. *Journal of Geophysical Research (Space Physics)*, *125*(3), e27583. https://doi.org/10.1029/2019JA027583

Agapitov, O. V., Artemyev, A., Krasnoselskikh, V., Khotyaintsev, Y. V., Mourenas, D., Breuillard, H., et al. (2013). Statistics of whistler mode waves in the outer radiation belt: Cluster STAFF-SA measurements. *Journal of Geophysical Research*, *118*(6), 3407–3420. https://doi.org/10.1002/jgra.50312

Angelopoulos, V. (2008). The THEMIS mission. *Space Science Reviews*, *141*(1–4), 5–34. https://doi.org/10.1007/s11214-008-9336-1

Angelopoulos, V., Cruce, P., Drozdov, A., Grimes, E. W., Hatzigeorgiu, N., King, D. A., et al. (2019). The space physics environment data analysis system (SPEDAS). *Space Science Reviews*, *215*(1), 9. https://doi.org/10.1007/s11214-018-0576-4

Angelopoulos, V., Sibeck, D., Carlson, C. W., McFadden, J. P., Larson, D., Lin, R. P., et al. (2008). First results from the THEMIS mission. *Space Science Reviews*, *141*(1–4), 453–476. https://doi.org/10.1007/s11214-008-9378-4

Angelopoulos, V., Tsai, E., Bingley, L., Shaffer, C., Turner, D. L., Runov, A., et al. (2020). The ELFIN mission. *Space Science Reviews*, *216*(5), 103. https://doi.org/10.1007/s11214-020-00721-7

Artemyev, A. V., Angelopoulos, V., Zhang, X. J., Runov, A., Petrukovich, A., Nakamura, R., et al. (2022). Thinning of the magnetotail current sheet inferred from low-altitude observations of energetic electrons. *Journal of Geophysical Research (Space Physics)*, *127*(10), e2022JA030705. https://doi.org/10.1029/2022JA030705

Auster, H. U., Glassmeier, K. H., Magnes, W., Aydogar, O., Baumjohann, W., Constantinescu, D., et al. (2008). The THEMIS fluxgate magnetometer. *Space Science Reviews*, *141*(1–4), 235–264. https://doi.org/10.1007/s11214-008-9365-9

Baker, D. N., Pulkkinen, T. I., Angelopoulos, V., Baumjohann, W., & McPherron, R. L. (1996). Neutral line model of substorms: Past results and present view. *Journal of Geophysical Research*, *101*(A6), 12975–13010. https://doi.org/10.1029/95JA03753

Beharrell, M. J., Honary, F., Rodger, C. J., & Clilverd, M. A. (2015). Substorm-induced energetic electron precipitation: Morphology and prediction. *Journal of Geophysical Research (Space Physics)*, *120*(4), 2993–3008. https://doi.org/10.1002/2014JA020632

Bekerat, H. A., Schunk, R. W., & Scherliess, L. (2007). Estimation of the high-latitude topside electron heat flux using DMSP plasma density measurements. *Journal of Atmospheric and Solar-Terrestrial Physics*, *69*(9), 1029–1048. https://doi.org/10.1016/j.jastp.2007.03.015

Birn, J., Runov, A., & Khotyaintsev, Y. (2021). Magnetotail processes. In R. Maggiolo, N. André, H. Hasegawa, & D. T. Welling (Eds.), *Magnetospheres in the solar system* (Vol. 2, pp. 245–275). https://doi.org/10.1002/9781119815624.ch17

Bland, E., Bozóki, T., & Partamies, N. (2022). Spatial extent of the energetic electron precipitation region during substorms. *Frontiers in Astronomy and Space Sciences*, *9*, 978371. https://doi.org/10.3389/fspas.2022.978371

Bland, E., Tesema, F., & Partamies, N. (2021). D-region impact area of energetic electron precipitation during pulsating aurora. *Annales Geophysicae*, *39*(1), 135–149. https://doi.org/10.5194/angeo-39-135-2021

Bonnell, J. W., Mozer, F. S., Delory, G. T., Hull, A. J., Ergun, R. E., Cully, C. M., et al. (2008). The electric field instrument (EFI) for THEMIS. *Space Science Reviews*, *141*(1–4), 303–341. https://doi.org/10.1007/s11214-008-9469-2

Boudouridis, A., Rodriguez, J. V., Kress, B. T., Dichter, B. K., & Onsager, T. G. (2020). Development of a Bowtie Inversion Technique for real-time processing of the GOES-16/-17 SEISS MPS-HI electron channels. *Space Weather*, *18*(4), e02403. https://doi.org/10.1029/2019SW002403

Califf, S., Zhao, H., Gkioulidou, M., Manweiler, J. W., Mitchell, D. G., & Tian, S. (2022). Multi-event study on the connection between subauroral polarization streams and deep energetic particle injections in the inner magnetosphere. *Journal of Geophysical Research (Space Physics)*, *127*(2), e2021JA029895. https://doi.org/10.1029/2021JA029895

Capannolo, L., Li, W., Millan, R., Smith, D., Sivadas, N., Sample, J., & Shekhar, S. (2022). Relativistic electron precipitation near midnight: Drivers, distribution, and properties. *Journal of Geophysical Research (Space Physics)*, *127*(1), e30111. https://doi.org/10.1029/2021JA030111

Chapman-Smith, K., Seppälä, A., Rodger, C. J., Hendy, A., & Forsyth, C. (2023). Observed loss of polar mesospheric ozone following substorm-driven electron precipitation. *Geophysical Research Letters*, *50*(17), e2023GL104860. https://doi.org/10.1029/2023GL104860

Chen, H., Gao, X., Lu, Q., & Tsurutani, B. T. (2023). Global distribution of relativistic electron precipitation and the dependences on substorm injection and solar wind ram pressure: Long-term POES observations. *Journal of Geophysical Research (Space Physics)*, *128*(11), e2023JA031566. https://doi.org/10.1029/2023JA031566

Chen, Z., Tian, H., Li, H., Tang, R., Ouyang, Z., & Deng, X. (2023). The study on the global evolution of energetic electron precipitation during geomagnetic storm based on deep learning algorithm. *Journal of Geophysical Research (Space Physics)*, *128*(3), e2022JA030974. https://doi.org/10.1029/2022JA030974

Coster, A., Williams, J., Weatherwax, A., Rideout, W., & Herne, D. (2013). Accuracy of GPS total electron content: GPS receiver bias temperature dependence. *Radio Science*, *48*(2), 190–196. https://doi.org/10.1002/rds.20011

Cresswell-Moorcock, K., Rodger, C. J., Kero, A., Collier, A. B., Clilverd, M. A., Häggström, I., & Pitkänen, T. (2013). A reexamination of latitudinal limits of substorm-produced energetic electron precipitation. *Journal of Geophysical Research (Space Physics)*, *118*(10), 6694–6705. https://doi.org/10.1002/jgra.50598

Dichter, B. K., Galica, G. E., McGarity, J. O., Tsui, S., Golightly, M. J., Lopate, C., & Connell, J. J. (2015). Specification, design, and calibration of the space weather suite of instruments on the NOAA GOES-R program spacecraft. *IEEE Transactions on Nuclear Science*, *62*(6), 2776–2783. https://doi.org/10.1109/TNS.2015.2477997

Dubyagin, S., Sergeev, V. A., & Kubyshkina, M. V. (2002). On the remote sensing of plasma sheet from low-altitude spacecraft. *Journal of Atmospheric and Solar-Terrestrial Physics*, *64*(5–6), 567–572. https://doi.org/10.1016/S1364-6826(02)00014-7

Evans, D. S., & Greer, M. S. (2004). Polar orbiting environmental satellite space environment monitor-2: Instrument description and archive data documentation.

Fang, X., Randall, C. E., Lummerzheim, D., Wang, W., Lu, G., Solomon, S. C., & Frahm, R. A. (2010). Parameterization of monoenergetic electron impact ionization. *Geophysical Research Letters*, *37*(22), L22106. https://doi.org/10.1029/2010GL045406

Foster, J. C., & Vo, H. B. (2002). Average characteristics and activity dependence of the subauroral polarization stream. *Journal of Geophysical Research (Space Physics)*, *107*(A12), 1475. https://doi.org/10.1029/2002JA009409

Gabrielse, C., Angelopoulos, V., Runov, A., & Turner, D. L. (2014). Statistical characteristics of particle injections throughout the equatorial magnetotail. *Journal of Geophysical Research*, *119*(4), 2512–2535. https://doi.org/10.1002/2013JA019638

Gabrielse, C., Kaeppler, S. R., Lu, G., Wang, C.-P., & Yu, Y. (2022). Energetic particle dynamics, precipitation, and conductivity. In Y. Nishimura, O. Verkhoglyadova, Y. Deng, & S.-R. Zhang (Eds.), *Cross-scale coupling and energy transfer in the magnetosphere-ionosphere-thermosphere system* (pp. 217–300). https://doi.org/10.1016/B978-0-12-821366-7.00002-0

Gabrielse, C., Spanswick, E., Artemyev, A., Nishimura, Y., Runov, A., Lyons, L., et al. (2019). Utilizing the Heliophysics/Geospace System Observatory to understand particle injections: Their scale sizes and propagation directions. *Journal of Geophysical Research (Space Physics)*, *124*(7), 5584–5609. https://doi.org/10.1029/2018JA025588

Galperin, Y. I., Ponomarev, V. N., & Zosimova, A. G. (1973). Direct measurements of drift velocity of ions in the upper ionosphere during a magnetic storm. I. Methodical questions and some results of measurements during a magnetically quiet period of time. *Kosmicheskie Issledovaniia*, *11*, 273–283.

Gan, L., Artemyev, A., Li, W., Zhang, X.-J., Ma, Q., Mourenas, D., et al. (2023). Bursty energetic electron precipitation by high-order resonance with very-oblique whistler-mode waves. *Geophysical Research Letters*, *50*(8), e2022GL101920. https://doi.org/10.1029/2022GL101920

Gkioulidou, M., Wang, C.-P., Wing, S., Lyons, L. R., Wolf, R. A., & Hsu, T.-S. (2012). Effect of an MLT dependent electron loss rate on the magnetosphere-ionosphere coupling. *Journal of Geophysical Research*, *117*(A11), 11218. https://doi.org/10.1029/2012JA018032

Green, J. L. (2013). Meped telescope data processing algorithm theoretical basis document.

He, F., Zhang, X.-X., & Chen, B. (2014). Solar cycle, seasonal, and diurnal variations of subauroral ion drifts: Statistical results. *Journal of Geophysical Research (Space Physics)*, *119*(6), 5076–5086. https://doi.org/10.1002/2014JA019807

Heelis, R. A., & Maute, A. (2020). Challenges to understanding the Earth's ionosphere and thermosphere. *Journal of Geophysical Research (Space Physics)*, *125*(7), e27497. https://doi.org/10.1029/2019JA027497

Heilig, B., Stolle, C., Kervalishvili, G., Rauberg, J., Miyoshi, Y., Tsuchiya, F., et al. (2022). Relation of the plasmapause to the midlatitude ionospheric trough, the sub-auroral temperature enhancement and the distribution of small-scale field aligned currents as observed in the magnetosphere by THEMIS, RBSP, and arase, and in the topside ionosphere by Swarm. *Journal of Geophysical Research (Space Physics)*, *127*(3), e29646. https://doi.org/10.1029/2021JA029646

Hendry, A. T., Seppälä, A., Rodger, C. J., & Clilverd, M. A. (2021). Impact of EMIC wave driven electron precipitation on the radiation belts and the atmosphere. *Journal of Geophysical Research (Space Physics)*, *126*(3), e28671. https://doi.org/10.1029/2020JA028671

Horvath, I., & Lovell, B. C. (2023). Abnormal sub-auroral ion drifts (ASAID) developed in the postmidnight (1-4) magnetic local time sector in 2013. *Journal of Geophysical Research (Space Physics)*, *128*(9), e2023JA031808. https://doi.org/10.1029/2023JA031808

Huang, C. (2021). Magnetospheric energy input to the ionosphere. In C. Huang & G. Lu (Eds.), *Ionosphere dynamics and applications* (Vol. 3, pp. 3–20). https://doi.org/10.1002/9781119815617.ch1
Huang, C.-S., Zhang, Y., Wang, W., Lin, D., & Wu, Q. (2021). Low-latitude zonal ion drifts and their relationship with subauroral polarization streams and auroral return flows during intense magnetic storms. *Journal of Geophysical Research: Space Physics*, *126*(12), e30001. https://doi.org/10.1029/2021JA030001
Jordanova, V. K., Morley, S. K., Engel, M. A., Godinez, H. C., Yakymenko, K., Henderson, M. G., et al. (2023). The RAM-SCB model and its applications to advance space weather forecasting. *Advances in Space Research*, *72*(12), 5596–5606. https://doi.org/10.1016/j.asr.2022.08.077
Khazanov, G. V., Glocer, A., & Chu, M. (2020). The Formation of electron heat flux in the region of diffuse aurora. *Journal of Geophysical Research: Space Physics*, *125*(8), e28175. https://doi.org/10.1029/2020JA028175
Khazanov, G. V., Robinson, R. M., Zesta, E., Sibeck, D. G., Chu, M., & Grubbs, G. A. (2018). Impact of precipitating electrons and magnetosphere-ionosphere coupling processes on ionospheric conductance. *Space Weather*, *16*(7), 829–837. https://doi.org/10.1029/2018SW001837
Khazanov, G. V., Sibeck, D. G., & Chu, M. (2021). Magnetosphere-ionosphere coupling of precipitating electrons and ionospheric conductance. In R. Maggiolo, N. André, H. Hasegawa, & D. T. Welling (Eds.), *Magnetospheres in the solar system* (Vol. 2, pp. 229–242). https://doi.org/10.1002/9781119815624.ch16
King, J. H., & Papitashvili, N. E. (2005). Solar wind spatial scales in and comparisons of hourly Wind and ACE plasma and magnetic field data. *Journal of Geophysical Research*, *110*(A2), A02104. https://doi.org/10.1029/2004JA010649
Knudsen, D. J., Burchill, J. K., Buchert, S. C., Eriksson, A. I., Gill, R., Wahlund, J. E., et al. (2017). Thermal ion imagers and Langmuir probes in the Swarm electric field instruments. *Journal of Geophysical Research (Space Physics)*, *122*(2), 2655–2673. https://doi.org/10.1002/2016JA022571
Lejosne, S., Kunduri, B. S. R., Mozer, F. S., & Turner, D. L. (2018). Energetic electron injections deep into the inner magnetosphere: A result of the subauroral polarization stream (SAPS) potential drop. *Geophysical Research Letters*, *45*(9), 3811–3819. https://doi.org/10.1029/2018GL077969
Lin, D., Wang, W., Merkin, V. G., Huang, C., Oppenheim, M., Sorathia, K., et al. (2022). Origin of dawnside subauroral polarization streams during major geomagnetic storms. *AGU Advances*, *3*(4), e2022AV000708. https://doi.org/10.1029/2022AV000708
Liu, J., Lyons, L. R., Wang, C.-P., Hairston, M. R., Zhang, Y., & Zou, Y. (2020). Dawnside auroral polarization streams. *Journal of Geophysical Research: Space Physics*, *125*(8), e27742. https://doi.org/10.1029/2019JA027742
Lomidze, L., Knudsen, D. J., Burchill, J., Kouznetsov, A., & Buchert, S. C. (2018). Calibration and validation of Swarm plasma densities and electron temperatures using ground-based radars and satellite radio occultation measurements. *Radio Science*, *53*(1), 15–36. https://doi.org/10.1002/2017RS006415
Lyons, L. R., Nishimura, Y., Zhang, S., Coster, A., Liu, J., Bristow, W. A., et al. (2021). Direct connection between auroral oval streamers/flow channels and equatorward traveling ionospheric disturbances. *Frontiers in Astronomy and Space Sciences*, *8*, 169. https://doi.org/10.3389/fspas.2021.738507
McFadden, J. P., Carlson, C. W., Larson, D., Ludlam, M., Abiad, R., Elliott, B., et al. (2008). The THEMIS ESA plasma instrument and in-flight calibration. *Space Science Reviews*, *141*(1–4), 277–302. https://doi.org/10.1007/s11214-008-9440-2
Meredith, N. P., Horne, R. B., Sicard-Piet, A., Boscher, D., Yearby, K. H., Li, W., & Thorne, R. M. (2012). Global model of lower band and upper band chorus from multiple satellite observations. *Journal of Geophysical Research*, *117*(A10), 10225. https://doi.org/10.1029/2012JA017978
Mironova, I. A., Artamonov, A. A., Bazilevskaya, G. A., Rozanov, E. V., Kovaltsov, G. A., Makhmutov, V. S., et al. (2019). Ionization of the polar atmosphere by energetic electron precipitation retrieved from balloon measurements. *Geophysical Research Letters*, *46*(2), 990–996. https://doi.org/10.1029/2018GL079421
Mishin, E., & Streltsov, A. (2021). Mesoscale and small-scale structure of the subauroral geospace. In C. Huang & G. Lu (Eds.), *Ionosphere dynamics and applications* (Vol. 3, pp. 139–158). https://doi.org/10.1002/9781119815617.ch8
Miyoshi, Y., Saito, S., Seki, K., Nishiyama, T., Kataoka, R., Asamura, K., et al. (2015). Relation between fine structure of energy spectra for pulsating aurora electrons and frequency spectra of whistler mode chorus waves. *Journal of Geophysical Research*, *120*(9), 7728–7736. https://doi.org/10.1002/2015JA021562
Mukhopadhyay, A., Welling, D., Liemohn, M., Ridley, A., Burleigh, M., Wu, C., et al. (2022). Global driving of auroral precipitation: 1. Balance of sources. *Journal of Geophysical Research (Space Physics)*, *127*(7), e30323. https://doi.org/10.1029/2022JA030323
Nakamura, R., Baumjohann, W., Klecker, B., Bogdanova, Y., Balogh, A., Rème, H., et al. (2002). Motion of the dipolarization front during a flow burst event observed by Cluster. *Geophysical Research Letters*, *29*(20), 200000–200001. https://doi.org/10.1029/2002GL015763
Newell, P. T., Liou, K., Zhang, Y., Sotirelis, T., Paxton, L. J., & Mitchell, E. J. (2014). OVATION Prime-2013: Extension of auroral precipitation model to higher disturbance levels. *Space Weather*, *12*(6), 368–379. https://doi.org/10.1002/2014SW001056
Newell, P. T., Sergeev, V. A., Bikkuzina, G. R., & Wing, S. (1998). Characterizing the state of the magnetosphere: Testing the ion precipitation maxima latitude (b2i) and the ion isotropy boundary. *Journal of Geophysical Research*, *103*(A3), 4739–4746. https://doi.org/10.1029/97JA03622
Newell, P. T., Sotirelis, T., Ruohoniemi, J. M., Carbary, J. F., Liou, K., Skura, J. P., et al. (2002). OVATION: Oval variation, assessment, tracking, intensity, and online nowcasting. *Annales Geophysicae*, *20*(7), 1039–1047. https://doi.org/10.5194/angeo-20-1039-2002
Newell, P. T., Sotirelis, T., & Wing, S. (2009). Diffuse, monoenergetic, and broadband aurora: The global precipitation budget. *Journal of Geophysical Research*, *114*(A9), A09207. https://doi.org/10.1029/2009JA014326
Nikolaev, A. V., Sergeev, V. A., Shukhtina, M. A., Spanswick, E., Rogov, D. D., & Stepanov, N. A. (2021). Study of substorm-related auroral absorption: Latitudinal width and factors affecting the peak intensity of energetic electron precipitation. *Journal of Geophysical Research: Space Physics*, *126*(12), e29779. https://doi.org/10.1029/2021JA029779
Nishimura, Y., Bortnik, J., Li, W., Thorne, R. M., Ni, B., Lyons, L. R., et al. (2013). Structures of dayside whistler-mode waves deduced from conjugate diffuse aurora. *Journal of Geophysical Research*, *118*(2), 664–673. https://doi.org/10.1029/2012JA018242
Nishimura, Y., Deng, Y., Lyons, L. R., McGranaghan, R. M., & Zettergren, M. D. (2021). Multiscale dynamics in the high-latitude ionosphere. In C. Huang & G. Lu (Eds.), *Ionosphere dynamics and applications* (Vol. 3, pp. 49–65). https://doi.org/10.1002/9781119815617.ch3
Nishimura, Y., Hussein, A., Erickson, P. J., Gallardo-Lacourt, B., & Angelopoulos, V. (2022). Statistical study of magnetospheric conditions for SAPS and SAID. *Geophysical Research Letters*, *49*(9), e98469. https://doi.org/10.1029/2022GL098469
Olsen, N., Friis-Christensen, E., Floberghagen, R., Alken, P., Beggan, C. D., Chulliat, A., et al. (2013). The Swarm satellite constellation application and research facility (SCARF) and Swarm data products. *Earth Planets and Space*, *65*(11), 1189–1200. https://doi.org/10.5047/eps.2013.07.001
Oyama, S., Kero, A., Rodger, C. J., Clilverd, M. A., Miyoshi, Y., Partamies, N., et al. (2017). Energetic electron precipitation and auroral morphology at the substorm recovery phase. *Journal of Geophysical Research Space Physics*, *122*(6), 6508–6527. https://doi.org/10.1002/2016JA023484

Pryse, S. E., Kersley, L., Malan, D., & Bishop, G. J. (2006). Parameterization of the main ionospheric trough in the European sector. *Radio Science*, *41*(5), RS5S14. https://doi.org/10.1029/2005RS003364

Rideout, W., & Coster, A. (2006). Automated GPS processing for global total electron content data. *GPS Solutions*, *10*(3), 219–228. https://doi.org/10.1007/s10291-006-0029-5

Rodger, A. (2008). The mid-latitude trough—Revisited. In *Washington DC American Geophysical Union geophysical monograph series* (Vol. 181, pp. 25–33). https://doi.org/10.1029/181GM04

Rodger, C. J., Clilverd, M. A., Hendry, A. T., & Forsyth, C. (2022). Examination of radiation belt dynamics during substorm clusters: Magnetic local time variation and intensity of precipitating fluxes. *Journal of Geophysical Research: Space Physics*, *127*(12), e2022JA030750. https://doi.org/10.1029/2022JA030750

Seppälä, A., Clilverd, M. A., Beharrell, M. J., Rodger, C. J., Verronen, P. T., Andersson, M. E., & Newnham, D. A. (2015). Substorm-induced energetic electron precipitation: Impact on atmospheric chemistry. *Geophysical Research Letters*, *42*(19), 8172–8176. https://doi.org/10.1002/2015GL065523

Sergeev, V. A., Angelopoulos, V., Kubyshkina, M., Donovan, E., Zhou, X.-Z., Runov, A., et al. (2011). Substorm growth and expansion onset as observed with ideal ground-spacecraft THEMIS coverage. *Journal of Geophysical Research*, *116*(A5), A00I26. https://doi.org/10.1029/2010JA015689

Sergeev, V. A., Chernyaev, I. A., Angelopoulos, V., & Ganushkina, N. Y. (2015). Magnetospheric conditions near the equatorial footpoints of proton isotropy boundaries. *Annales Geophysicae*, *33*(12), 1485–1493. https://doi.org/10.5194/angeo-33-1485-2015

Sergeev, V. A., Gordeev, E. I., Merkin, V. G., & Sitnov, M. I. (2018). Does a local B-minimum appear in the tail current sheet during a substorm growth phase? *Geophysical Research Letters*, *45*(6), 2566–2573. https://doi.org/10.1002/2018GL077183

Sergeev, V. A., Nishimura, Y., Kubyshkina, M., Angelopoulos, V., Nakamura, R., & Singer, H. (2012). Magnetospheric location of the equatorward prebreakup arc. *Journal of Geophysical Research*, *117*(A1), A01212. https://doi.org/10.1029/2011JA017154

Sergeev, V. A., Shukhtina, M. A., Stepanov, N. A., Rogov, D. D., Nikolaev, A. V., Spanswick, E., et al. (2020). Toward the reconstruction of substorm-related dynamical pattern of the radiowave auroral absorption. *Space Weather*, *18*(3), e02385. https://doi.org/10.1029/2019SW002385

Shinbori, A., Otsuka, Y., Tsugawa, T., Nishioka, M., Kumamoto, A., Tsuchiya, F., et al. (2021). Relationship between the locations of the midlatitude trough and plasmapause using GNSS TEC and arase satellite observation data. *Journal of Geophysical Research: Space Physics*, *126*(5), e28943. https://doi.org/10.1029/2020JA028943

Shprits, Y. Y., Subbotin, D. A., Meredith, N. P., & Elkington, S. R. (2008). Review of modeling of losses and sources of relativistic electrons in the outer radiation belt II: Local acceleration and loss. *Journal of Atmospheric and Solar-Terrestrial Physics*, *70*(14), 1694–1713. https://doi.org/10.1016/j.jastp.2008.06.014

Sitnov, M. I., Birn, J., Ferdousi, B., Gordeev, E., Khotyaintsev, Y., Merkin, V., et al. (2019). Explosive magnetotail activity. *Space Science Review*, *215*(4), 31. https://doi.org/10.1007/s11214-019-0599-5

Sivadas, N., Semeter, J., Nishimura, Y., & Kero, A. (2017). Simultaneous measurements of substorm-related electron energization in the ionosphere and the plasma sheet. *Journal of Geophysical Research: Space Physics*, *122*(10), 10528–10547. https://doi.org/10.1002/2017JA023995

Sivadas, N., Semeter, J., Nishimura, Y., & Mrak, S. (2019). Optical signatures of the outer radiation belt boundary. *Geophysical Research Letters*, *46*(15), 8588–8596. https://doi.org/10.1029/2019GL083908

Sorathia, K. A., Michael, A., Merkin, V. G., Ukhorskiy, A. Y., Turner, D. L., Lyon, J. G., et al. (2021). The role of mesoscale plasma sheet dynamics in ring current formation. *Frontiers in Astronomy and Space Sciences*, *8*, 192. https://doi.org/10.3389/fspas.2021.761875

Spiro, R. W., Heelis, R. A., & Hanson, W. B. (1978). Ion convection and the formation of the mid-latitude F region ionization trough. *Journal of Geophysical Research*, *83*(A9), 4255–4264. https://doi.org/10.1029/JA083iA09p04255

Stepanov, N. A., Sergeev, V. A., Shukhtina, M. A., Ogawa, Y., Chu, X., & Rogov, D. D. (2021). Ionospheric electron density and conductance changes in the auroral zone during substorms. *Journal of Geophysical Research: Space Physics*, *126*(7), e29572. https://doi.org/10.1029/2021JA029572

Summers, D., & Thorne, R. M. (2003). Relativistic electron pitch-angle scattering by electromagnetic ion cyclotron waves during geomagnetic storms. *Journal of Geophysical Research*, *108*(A4), 1143. https://doi.org/10.1029/2002JA009489

Tesema, F., Partamies, N., Tyssøy, H. N., Kero, A., & Smith-Johnsen, C. (2020). Observations of electron precipitation during pulsating aurora and its chemical impact. *Journal of Geophysical Research (Space Physics)*, *125*(6), e27713. https://doi.org/10.1029/2019JA027713

Thorne, R. M., Bortnik, J., Li, W., & Ma, Q. (2021). Wave–particle interactions in the earth's magnetosphere. In *Magnetospheres in the solar system* (pp. 93–108). American Geophysical Union (AGU). https://doi.org/10.1002/9781119815624.ch6

Thorne, R. M., Ni, B., Tao, X., Horne, R. B., & Meredith, N. P. (2010). Scattering by chorus waves as the dominant cause of diffuse auroral precipitation. *Nature*, *467*(7318), 943–946. https://doi.org/10.1038/nature09467

Tsai, E., Artemyev, A., Zhang, X.-J., & Angelopoulos, V. (2022). Relativistic electron precipitation driven by nonlinear resonance with whistler-mode waves. *Journal of Geophysical Research: Space Physics*, *127*(5), e30338. https://doi.org/10.1029/2022JA030338

Turunen, E., Kero, A., Verronen, P. T., Miyoshi, Y., Oyama, S.-I., & Saito, S. (2016). Mesospheric ozone destruction by high-energy electron precipitation associated with pulsating aurora. *Journal of Geophysical Research: Atmospheres*, *121*(19), 11852–11861. https://doi.org/10.1002/2016JD025015

Verronen, P. T., Kero, A., Partamies, N., Szeląg, M. E., Oyama, S.-I., Miyoshi, Y., & Turunen, E. (2021). Simulated seasonal impact on middle atmospheric ozone from high-energy electron precipitation related to pulsating aurorae. *Annales Geophysicae*, *39*(5), 883–897. https://doi.org/10.5194/angeo-39-883-2021

Vierinen, J., Coster, A. J., Rideout, W. C., Erickson, P. J., & Norberg, J. (2015). Statistical framework for estimating GNSS bias. In *Atmospheric measurement techniques discussions* (Vol. 8, pp. 9373–9398). https://doi.org/10.5194/amtd-8-9373-2015

Vo, H. B., & Foster, J. C. (2001). A quantitative study of ionospheric density gradients at midlatitudes. *Journal of Geophysical Research*, *106*(A10), 21555–21564. https://doi.org/10.1029/2000JA000397

Yahnin, A. G., Sergeev, V. A., Gvozdevsky, B. B., & Vennerstrøm, S. (1997). Magnetospheric source region of discrete auroras inferred from their relationship with isotropy boundaries of energetic particles. *Annales Geophysicae*, *15*(8), 943–958. https://doi.org/10.1007/s00585-997-0943-z

Yahnin, A. G., Yahnina, T. A., Raita, T., & Manninen, J. (2017). Ground pulsation magnetometer observations conjugated with relativistic electron precipitation. *Journal of Geophysical Research: Space Physics*, *122*(9), 9169–9182. https://doi.org/10.1002/2017JA024249

Yahnin, A. G., Yahnina, T. A., Semenova, N. V., Gvozdevsky, B. B., & Pashin, A. B. (2016). Relativistic electron precipitation as seen by NOAA POES. *Journal of Geophysical Research (Space Physics)*, *121*(9), 8286–8299. https://doi.org/10.1002/2016JA022765

Yizengaw, E., & Moldwin, M. B. (2005). The altitude extension of the mid-latitude trough and its correlation with plasmapause position. *Geophysical Research Letters*, *32*(9), L09105. https://doi.org/10.1029/2005GL022854

Young, S. L., Denton, R. E., Anderson, B. J., & Hudson, M. K. (2002). Empirical model for μ scattering caused by field line curvature in a realistic magnetosphere. *Journal of Geophysical Research*, *107*(A6), 1069. https://doi.org/10.1029/2000JA000294

Yu, Y., Cao, J., Pu, Z., Jordanova, V. K., & Ridley, A. (2022). Meso-scale electrodynamic coupling of the Earth magnetosphere-ionosphere system. *Space Science Reviews*, *218*(8), 74. https://doi.org/10.1007/s11214-022-00940-0

Yu, Y., Jordanova, V. K., McGranaghan, R. M., & Solomon, S. C. (2018). Self-consistent modeling of electron precipitation and responses in the ionosphere: Application to low-altitude energization during substorms. *Geophysical Research Letters*, *45*(13), 6371–6381. https://doi.org/10.1029/2018GL078828